

Design and performances of the Shack-Hartmann sensor within the Active Phasing Experiment

R. Mazzoleni ^{a*}, F. Gonté ^a, I. Surdej ^a, C. Araujo ^a, R. Brast ^a, F. Derie ^a, P. Duhoux ^a, C. Dupuy ^a,
C. Frank ^a, R. Karban ^a, L. Noethe ^a, N. Yaitskova ^a

^aEuropean Organisation for Astronomical Research in the Southern Hemisphere
Karl-Schwarzschild-Str. 2, Garching, Germany

ABSTRACT

The Shack-Hartmann Phasing Sensor (SHAPS) has been integrated in the Active Phasing Experiment (APE) at ESO. It is currently under test in the laboratory. The tests on sky are foreseen for the end of 2008, when APE will be mounted at the Nasmyth focus of one of the VLT unit telescopes. SHAPS is based on the Shack-Hartmann principle: the lenslet array is located in a plane which is optically conjugated to the Active Segmented Mirror (ASM) of APE and is composed of two types of microlenses, circular and cylindrical, which give information about the wavefront slope and the piston steps, respectively. This proceeding contains a description of SHAPS and of the algorithms implemented for the wavefront reconstruction and for the phasing. The preliminary results obtained during the laboratory tests are discussed and compared with the theoretical predictions. The performances of SHAPS at the VLT and at the European Extremely Large Telescope (E-ELT) are estimated.

Keywords: Shack-Hartmann sensor, phasing, segmented telescope, active optics, E-ELT.

1. INTRODUCTION

The wavefront provided by a segmented telescope needs to be flattened within a fraction of the wavelength to achieve the diffraction limit and fully exploit the capability of the telescope. Several types of wavefront sensors can be selected for the measurement of the phasing errors.

An experiment is currently running at ESO, namely the Active Phasing Experiment (APE, see [4] and [9]) with the scope to study and compare the performances of different kinds of phasing sensors. A segmented mirror will be conjugated to the primary mirror of the Very Large Telescope, and four different phasing sensors will be tested in the laboratory and on sky under identical conditions: a Shack-Hartmann Phasing Sensor (SHAPS), a Diffraction Image Phase Sensing Instrument (DIPSI), a Pyramid Phasing Sensor (PYPS) and the Zernike Unit for Segment phasing (ZEUS).

The segmented mirror is kept aligned and phased by means of an internal metrology system; in good conditions (stable temperature, no vibrations) it can guarantee an alignment of the full mirror which is less than 1.0 nm RMS in surface. APE is equipped with an internal calibration source which can simulate a point-like source with and without aberrations generated by atmospheric turbulence.

SHAPS is one of the wavefront sensors fed by APE. It can measure the wavefront slopes as in the classical Shack-Hartmann sensor (see [5]) but in addition also the piston step between adjacent segments, using a technique which has already been implemented in the Keck telescope (see [2]).

This paper is organized as follows. In Section 2 the new optical layout, the opto-mechanical design and the control system of SHAPS are described. In Section 3 the algorithms used in the wavefront analysis are described, showing how the information about the segment tip-tilts, the global aberrations and the piston steps are computed starting from the signal. In section 4 some results obtained during the preliminary tests performed in lab are presented. Finally in Section 5 the performance of SHAPS with APE installed at VLT is estimated and extrapolated to the E-ELT case. The conclusions are summarized in Section 6.

*R. Mazzoleni: E-mail: rmazzole@eso.org, Telephone: +49 89 3200 6561

2. SHAPS DESCRIPTION

2.1. The new optical layout.

Since its presentation in 2006 (see [3]), the optical layout of SHAPS has been slightly changed with the inclusion of a second arm and of a zooming unit just in front of the lenslet array; the new layout is shown in Figure 1.

The F/15 beam is delivered by APE to the SHAPS entrance. Neutral density filters and color filters are installed just behind the focal plane at the entrance of SHAPS. The beam is then collimated by a lens and divided in two beams by a beam-splitter (T=80%; R=20%):

- The reflected light goes to the camera used for the analysis of the APE Point Spread Function (PSF). An achromatic doublet with a focal distance of 300 mm is inserted after the intermediate pupil to focalize the beam. At the detector plane an F/45 beam is delivered with a scale of 5 milliarcsec/pixel. This camera is not needed by SHAPS for the wavefront analysis but it can be used for alignment checks.
- The transmitted light forms an intermediate pupil after a folding mirror. A zoom unit consisting of two achromatic doublets, which transfers this pupil into the plane of the micro-lenslet array, allows for a fine adjusting of the scale. The spots of the micro-lenslets are re-imaged on the detector by a relay unit composed of two achromatic doublets.

A calibration unit which provides an input beam with the same optical characteristics as the one delivered by APE, can be inserted on request. It is used for alignment and for internal calibration.

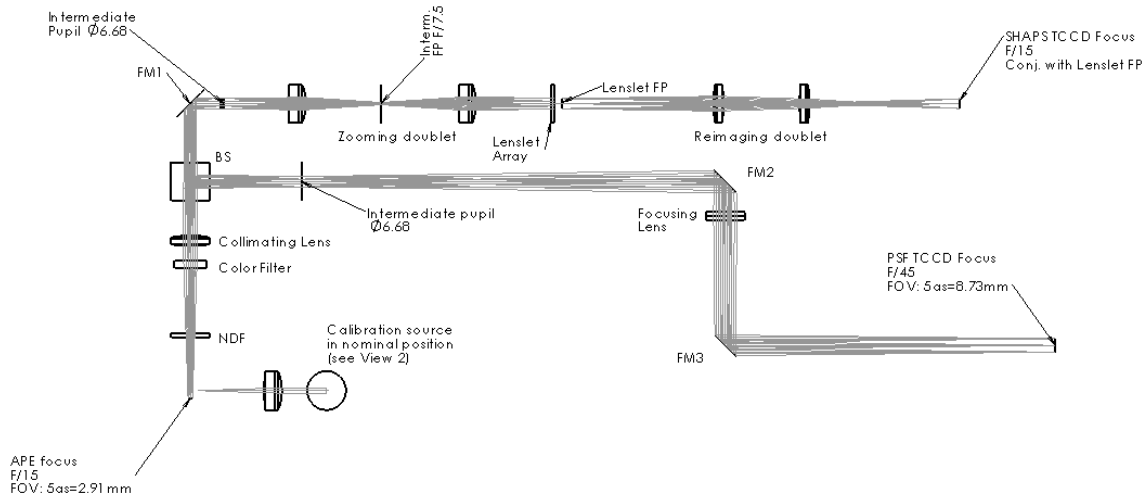


Figure 1: SHAPS optical layout.

The lenslet array has been slightly tilted by an angle of about 5° (this tilt is not shown in the optical design) in order to compensate a small but not negligible anamorphism ($\sim 1\%$) in the image of the pupil produced by the off-axis parabolic mirror which is in front of the segmented mirror in APE. As a consequence, the focal plane of the lenslet is tilted by the same angle and the same tilt has been applied to the detector.

2.2. Opto-mechanical description.

A picture of SHAPS without the protection panel and a 3-dimensional sketch view are shown in the Figure 2.

SHAPS is assembled on a $300 \times 900 \text{ mm}^2$ breadboard. The optical axis lies in a plane 130 mm above the surface of the breadboard. Custom mechanical supports have been manufactured to accommodate the optics.

The optical elements are mounted on the supports, aligned and fixed to the breadboard. Four manual micrometric adjustment are available for the accurate positioning of the micro-lenslet array (translation perpendicular and rotation around the optical axis are possible) and for the modification of the magnification of the ASM image on the lenslet plane.

The only optical element which has been custom manufactured for SHAPS is the micro-lenslet array. All other elements (lenses, mirrors and the beam-splitter) are standard commercial components.

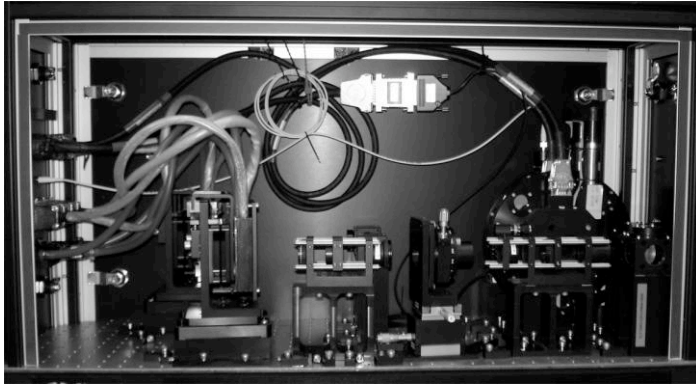
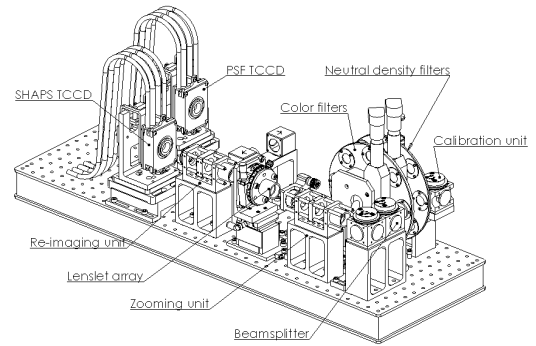


Figure 2: SHAPS mechanical layout



The micro-lenslet array is composed of $19 \times 61 = 1159$ circular lenslets, $\text{\O}150 \mu\text{m}$, and of 156 cylindrical lenslet, $150 \times 450 \mu\text{m}$, arranged according to the layout shown in Figure 3. Four samples of this array have been manufactured by SUSS MicroOptics (SWI). The diameter of one of the circular lenslet corresponds to a subaperture with a diameter of 189 mm on the primary mirror of VLT.

A set of 7 colored filters allows the selection of the wavelength in the range between 600nm to 900 nm, covering the wavelength range over which the CCDs are most efficient. A set of neutral density filters allows the selection of a source of different intensities, covering an interval of 10 magnitudes.

The following tables show the color and the neutral density filters installed in SHAPS:

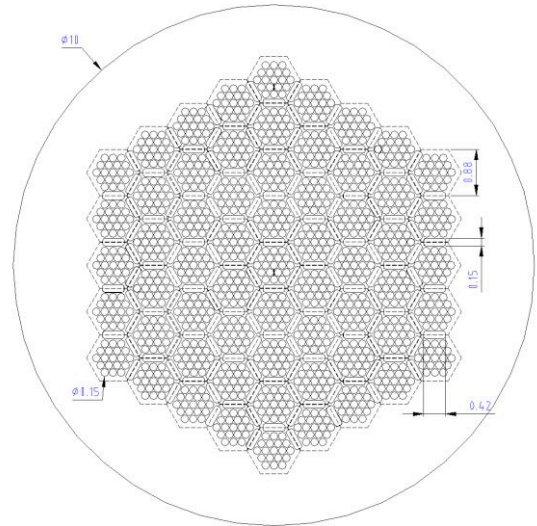


Figure 3: The lenslet array

Filter name	Central wavelength (nm)	Bandwidth (nm)
CF0	Window	
CF1	600	80
CF2	690	80
CF3	780	80
CF4	600	10
CF5	690	10
CF6	780	10
CF7	900	40

Filter name	Density
NDF0	0
NDF1	0.03
NDF2	0.2
NDF3	0.5
NDF4	1
NDF5	2
NDF6	4

The CCD used for SHAPS is of the type E2V 57-10, i.e. a frame transfer 512 x 512, configured in the Advanced Inverted Mode (AIMO). This mode reduces the dark current by a factor of approximately 70 with respect to the Non-AIMO which dramatically reduces the noise for long integration times. The CCD used for the PSF camera is a frame transfer 1024 x 1024 of the type E2V 47-20.

2.3. Control System.

The control system is based on the VLT standards and consists of two major parts, the coordination software, running on a Linux Workstation and the device control running on VxWorks VME crates, which use standard VLT control electronics.

To cope with the complexity of calibration and acquisition procedures and the flexibility required for tests in the laboratory and on sky, the control software was built using a code generation framework (see [1]).

The integration with the data analysis software is implemented using the abstraction of a dataset which allows flexible application of different algorithms to a number of images. The control and data analysis software have been already successfully integrated, tested and debugged.

The user interface allows the choice between different configurations of the hardware and analysis strategies. Figure 4 shows the main panel used to control SHAPS.

The main features of the software are:

- select the parameters that will be used during the acquisition (exposure time, color band, seeing);
- choose among different algorithm policies that will be used in the signal analysis;
- select the quantities that the user wants to measure: tip-tilt, piston or the low-order aberrations;
- define the type of calibration (dark current or piston / tip-tilt) and store the calibration images and parameters;
- decide if the measurement, using a certain reconstruction type, shall be applied to the segmented mirror;
- any combination of available calibration data can be used for acquisition.

The acquisition consists of setting up the SHAPS devices (the shutter, the internal calibration unit, the color filter wheel and the neutral density filter wheel) and recording the image with a technical CCD. The light source is selected by the user among two sources: the laser beam at 650nm and the halogen lamp which is, in general, used with one of the color filter.

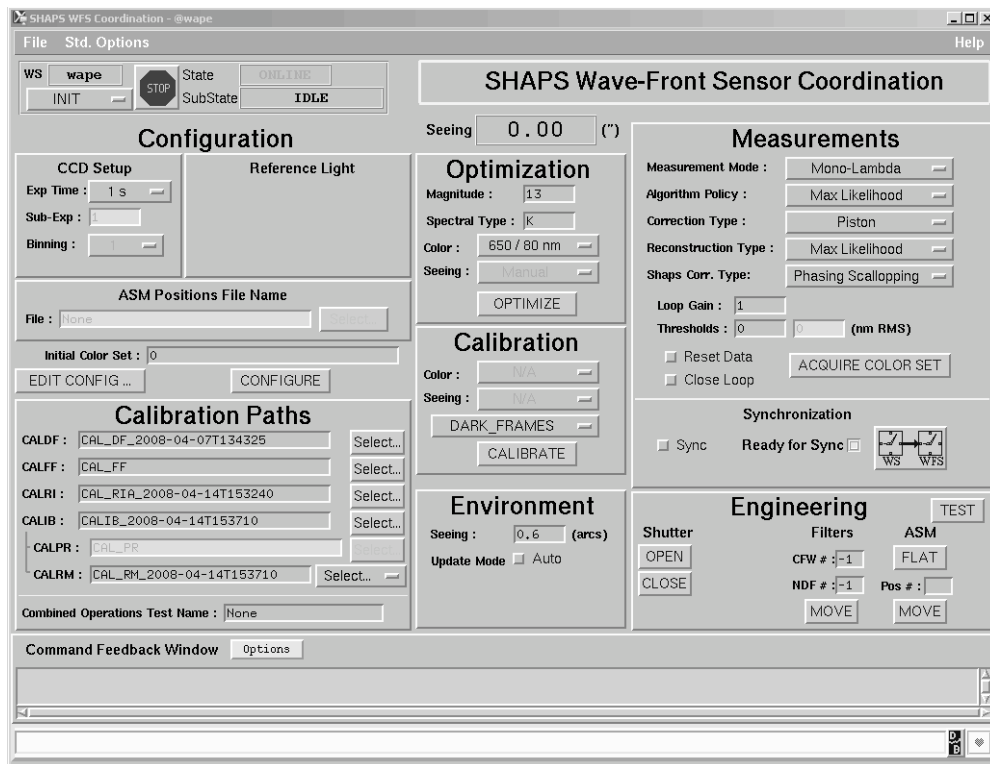


Figure 4: Control panel of SHAPS

Every image taken is automatically processed by the algorithms; it is stored, together with the results, in a specific scheme. This scheme is designed in such a way that any result can be reproduced offline by saving all the parameters describing the relevant environmental conditions and configurations, and the images in FITS format. The loop is closed by converting the measured piston / tip-tilt into voltage values and applying them to the ASM.

3. WAVEFRONT ANALYSIS ALGORITHM

3.1. Signal from the lenslet array.

One of the images acquired by SHAPS during the tests is shown in the Figure 5 on the left.

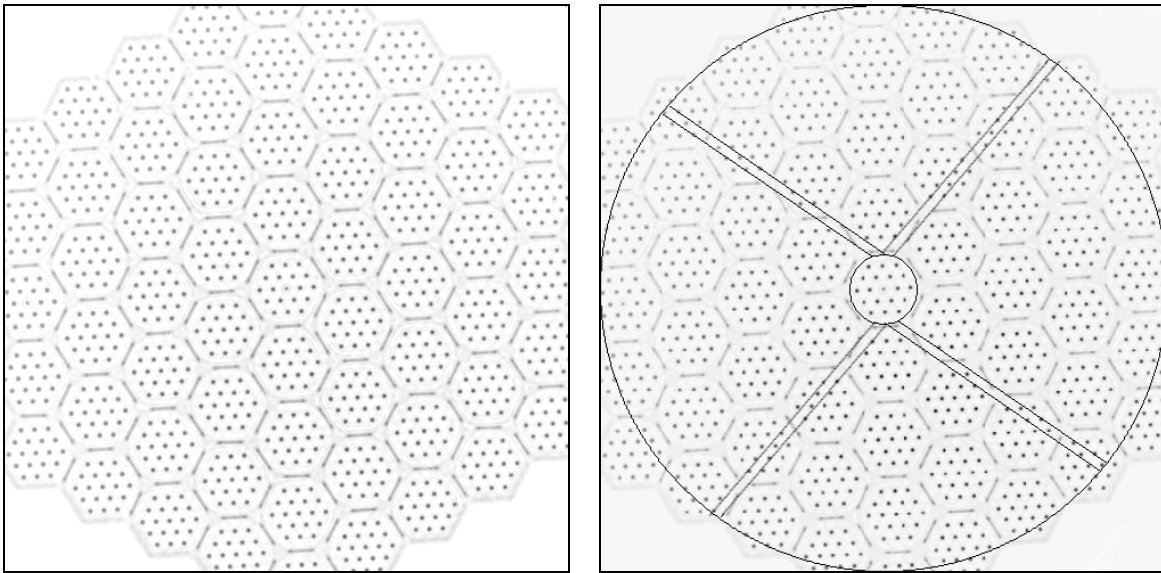


Figure 5: SHAPS image (left); on the right the image of the VLT pupil with the 4 spiders is outlined.

The border of the image corresponds to the size of the detector, a 512 x 512 pixels CCD.

The circular and the elongated spots are generated by the circular lenslets and the rectangular lenslets, respectively. The analysis software uses the circular spots to measure the low-order aberration (segment tip-tilt and low-order modes) and the rectangular spots to measure the segment pistons at segment borders. The two algorithms will be presented in the next sections.

In the image on the right hand side of Figure 5 the pupil of the VLT with the 4 spiders has been superimposed on the spot pattern. The small circle at the center of the image indicates the obscuration caused by the secondary mirror of the VL. It will almost completely hide the central segment which is supposed to be fixed. The big circle indicates the outer border of the pupil. Apparently, most of the external segments will be only partially illuminated. As a consequence, the detection of their tip-tilt values will be less accurate. The 4 spiders will also have a degrading effect because they will either eliminate or modify some of the spots.

The circular pupil as well as the 4 spiders can be emulated by a mask located in the APE calibration unit. This will permit to study their effects in the laboratory.

3.2. Wavefront reconstruction algorithm: tip-tilts and aberrations.

The shifts of the circular spots with respect to a reference image are used to compute the local wavefront tilt. In first approximation such shifts depend linearly on the wavefront error slope:

$$\delta_i(\bar{X}_j) = \partial_i W(\bar{X}_j) \cdot f, \quad (1)$$

where $\delta_i(x_j)$ is the displacement of the spot at x_j along the direction i , $\partial_i W(x_j)$ is the derivative of the wavefront error at the lenslet plane along the direction i at the coordinate x_j and f is the focal length of the Shack-Hartmann lenslet.

In the current configuration, a tilt of 1 arcsec of one segment of the ASM corresponds to a shift of the spot of approximately $1.5 \mu\text{m}$.

The displacement measured at each point can be represented as a 2-dimensional vectorial field, as shown in Figure 6.

The wavefront error slope can be represented by a finite summation of linearly independent modes:

$$\partial_i W(\bar{X}_j) = \sum_{n=0}^{M-1} a_n \partial_i Z_n(\bar{X}_j) + \sum_{m=0}^{M-1} \sum_{k=0}^{K-1} b_{mk} \partial_i S_{mk}(\bar{X}_j) \quad (2)$$

where $\{Z_n\}$ is a set of independent functions which describe the continuous modes (e.g. global defocus) and $\{S_{mk}\}$ is a set of independent functions which describe the non-continuous modes (e.g. tip-tilt of each segment).

By inverting the relation (2) and combining it with (1) it is possible to estimate the coefficients a_n and b_{mk} .

More detailed descriptions of the algorithm and of the problem faced in disentangling of non-orthogonal modes are in [6].

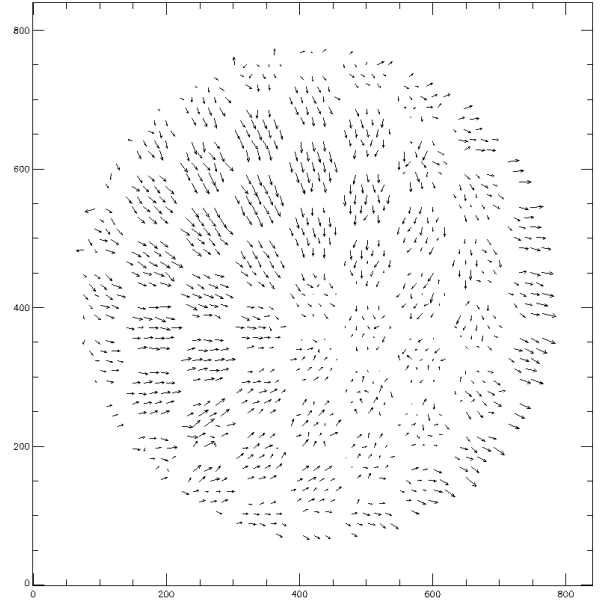


Figure 6: The vectorial field aberration measured by SHAPS.

3.3. Phasing: piston measurement / calibration / capture range.

The shape of the signal produced by a cylindrical lenslet can be used to determine the piston step at the border (see [7]). In the 1-dimensional case of a perfectly centered border the normalized intensity distribution can be expressed by the following formula:

$$p(\xi, \theta) = \frac{\left[\sin\left(\frac{\pi\xi}{\xi_0} + \frac{2\pi\theta}{\lambda}\right) - \sin\left(\frac{2\pi\theta}{\lambda}\right) \right]^2}{\left(\frac{\xi}{\xi_0} \right)^2}$$

where θ is the wavefront piston step in units of the wavelength λ , ξ is the spatial dimension and ξ_0 is a normalization unit given by

$$\xi_0 = \frac{\lambda}{a}$$

where $a = 150 \mu\text{m}$ is the lenslet width; $\xi = \xi_0$ corresponds to the position of the first zero of the diffraction pattern.

The plots in Figure 7 represent the

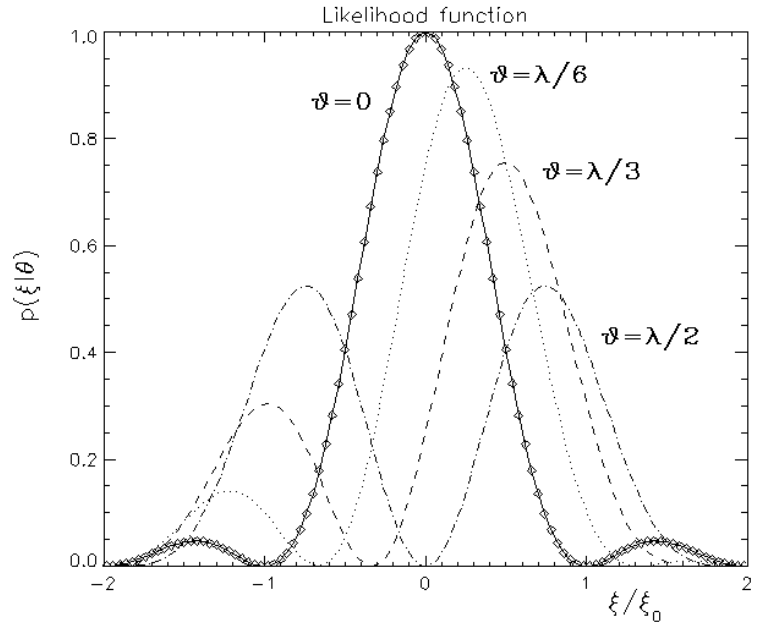


Figure 7: Signal shape at different piston steps.

intensity profile for 4 different values of the wavefront step $\theta = [0, \lambda/6, \lambda/3, \lambda/2]$.

Different methods have been investigated for the estimation of the piston step from the intensity profile. The most promising ones are based on the curve-fitting and on the maximum-likelihood estimation. The curve-fitting method is based on the Gauss–Newton algorithm and the free parameters are the amplitude, the piston step and the coordinate of the origin. The maximum-likelihood method is based on the correlation between the measured signal and the logarithm of the probability distributions associated with a set of piston steps. Around the maximum, the shape of the function representing the correlation is a parabola, with the maximum being located at the most likely value of the piston step. We start with 12 different piston steps, ranging from $-\lambda/2$ to $+\lambda/2$, and fit a parabola to the corresponding correlation data.

Although not strictly necessary, a calibration procedure has been foreseen. The segments belonging to the family #0 in Figure 8 remain fixed since the central segment is used as a reference and remains fixed. To all segments belonging to one of the families #1 and #2, 12 steps ranging from $-\lambda/2$ to $+\lambda/2$ are applied. The measured piston steps are the basis of the calibration curve.

One way of removing the 2π -ambiguity is a measurement of the piston step at different wavelength (at least 2, not integer multiples); and to find a value of the piston step which is compatible with all of these measurements. In this way the so called “capture range”, which is the wavelength interval within which the piston step can be determined without ambiguities, can be extended from $[-\lambda/2, -\lambda/2]$ to a few wavelengths, depending on the errors in each measurements.

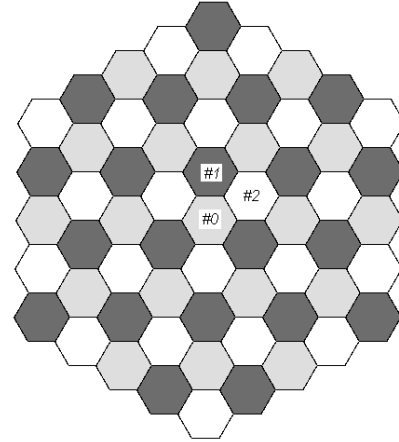


Figure 8: Families of segments.

The algorithm has been implemented and successfully tested using the wavelength 650nm, 700nm and 905 nm.

4. RESULTS

4.1. Wavefront aberrations.

During the alignment phase, a flat dummy mirror ($\lambda/10$ over $\varnothing 130\text{mm}$) was used to replace the ASM in order to have a flat reference. The picture and the histogram in Figure 9 show the values of the residual aberrations measured by SHAPS (in the picture on the left, the tip-tilt and defocus components have been removed).

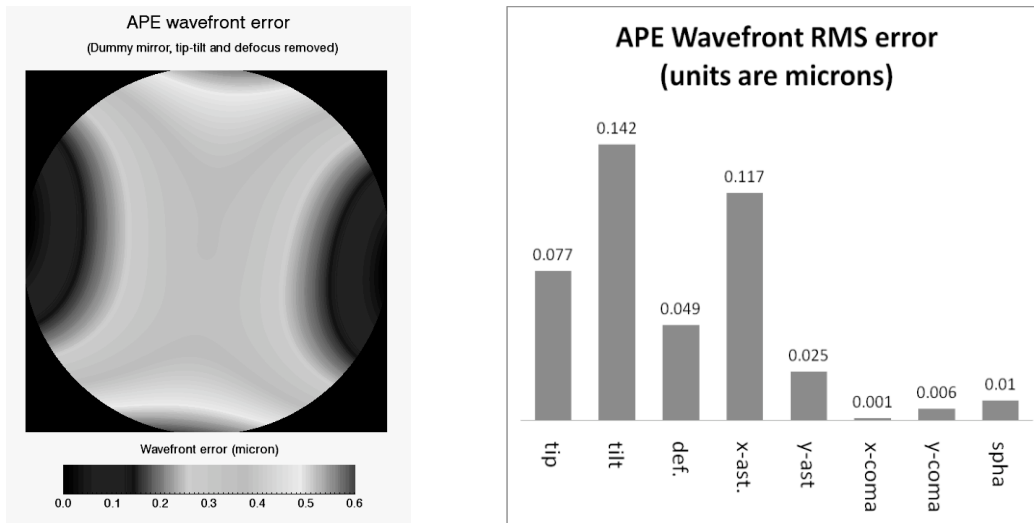


Figure 9: APE wavefront error measured by SHAPS with the dummy mirror inserted.

The APE wavefront errors with the dummy replacing the ASM are $1.07\mu\text{m PV}$ and $0.212\mu\text{m RMS}$. After removal of the tip-tilt and defocus components, the residual wavefront errors are $0.602\mu\text{m PV}$ and $0.121\mu\text{m RMS}$ and they are mostly due to the X component of the astigmatism.

4.2. Tip-tilt corrections

During the preliminary tests, the tip-tilts of the segments in the range $[0, 5]$ arcsec and the uncertainty of the measurements at different intensities have been measured. The results are shown in Figure 10.

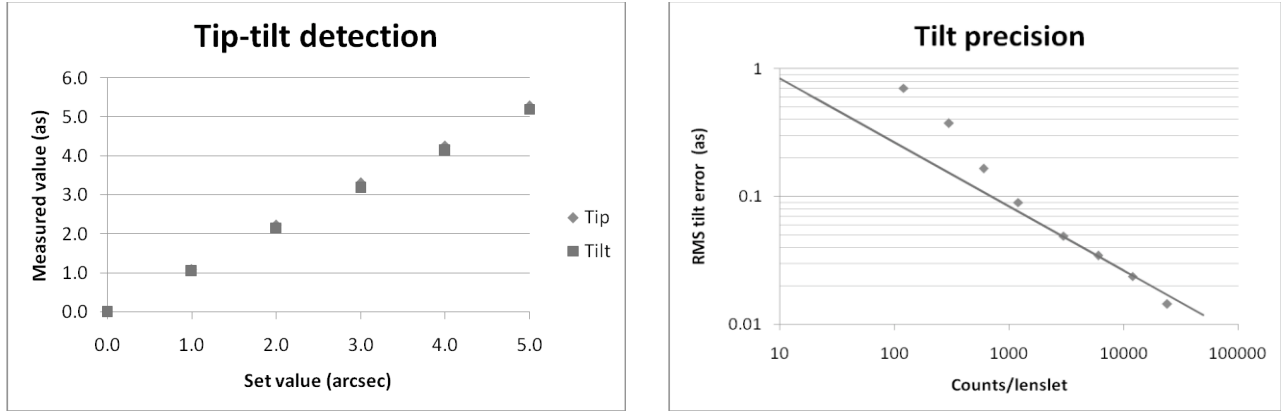
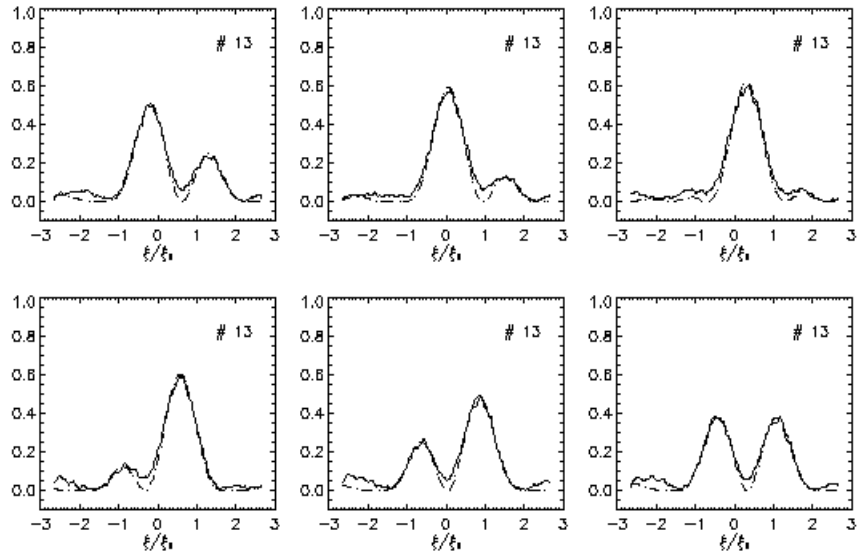


Figure 10: Detection of tip-tilt for segment #1 (left) and the expected precision (right); the points corresponds to the measurement and the line represents the theoretical limit (see section 5).

The accuracy in the tip-tilt detection is of the order of 2% and the uncertainty in the measure is in good agreement with the theoretical prediction for signal higher than 1000 counts/lenslet (see section 5 for the derivation of the theoretical prediction). At low-signal the noise of the detector is probably due to the detector noise. More tests are planned to study the tilt-precision under different conditions (source intensity, seeing).

4.3. Phasing measurement

The plots in Figure 11 show the normalized signal across the border #13 with six different wavefront piston steps ranging from $-\lambda/3$ to $\lambda/2$, with $\lambda=650\text{nm}$. The solid lines show the measured data and the dashed-dotted line the fitted curve which is a good representation of the measured data.



In Figure 12 the steps measured on the borders 0 to 9 when the family #1 of segments was lifted up by 50nm are shown. The values have been measured with 3 different methods: maximum likelihood estimation (MLE), curve-fitting (CFIT) and Sum-square method (SUMSQ).

This last method is based on the fact that the normalized integral of the square of the difference between the signal at a

Figure 11: Normalized signal across the border (continuous line) and its fitting (dashed-dotted line); piston varies between $[-108.4, 162.6]$ with steps of 54.2nm.

given piston step θ and the signal when the piston step is 0, is proportional to $\sin(2\pi\theta/\lambda)^2$:

$$2 \int |\rho(\xi, \theta) - \rho(\xi, 0)|^2 d\xi = \left(\sin \frac{2\pi\theta}{\lambda} \right)^2$$

This method can be easily implemented when the signal at step 0 is available.

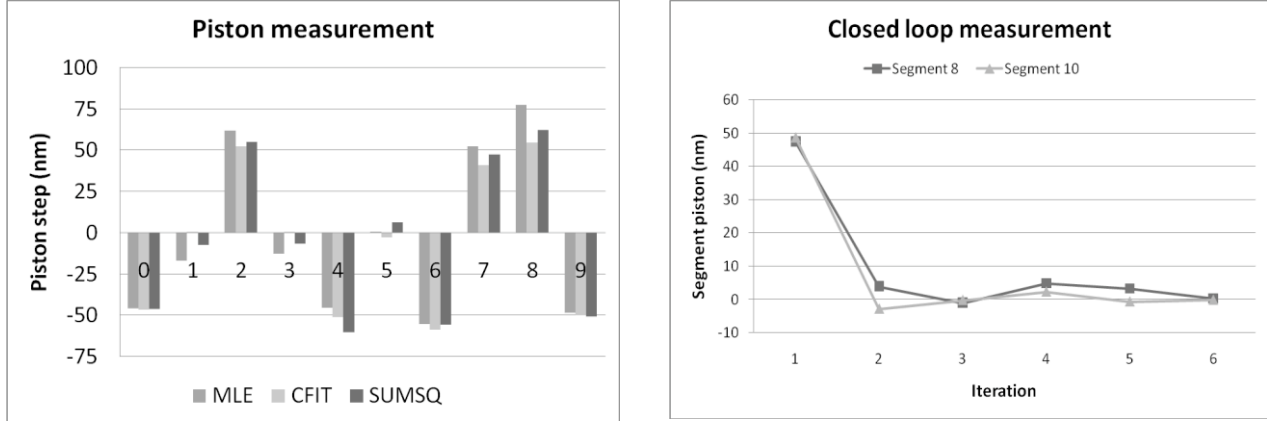


Figure 12: Piston measurements: 10 borders in open loop (left) and 2 segments in close loop (right).

The measurement error was of the order of a few nanometers. The most accurate method seems to be SUMSQ; followed by the MLE, but further analysis is necessary to confirm these results and to characterize the accuracy and the precision of each method.

On the right side of Figure 12 the piston steps of two segments (#8 and #10) during 6 iterations of a closed-loop correction cycle have been plotted. Already after the first measurement the piston steps are well corrected and the segment position is stable.

The agreement of the real curve with the theoretical one is not always satisfying like in the case just shown. The discrepancies might have many causes: the non-perfect alignment between the ASM and the lenslet array, the non-perfect flatness of the segments, the residual tilts of the adjacent segments. This matter is under investigation and it will be crucial in order to determine, for instance, the loss of sensitivity of this sensor due to misalignment and therefore the precision required for the alignment of the lenslet array.

4.4. Measurement using multi-wavelength technique

The signal at the borders changes with a periodicity of λ . The step measured in the mono-wavelength mode may therefore differ from the real step by a multiple of λ or 2π in radians. The measurements obtained at different wavelength can be used to remove this ambiguity (see [8] for a detailed description) and to extend the so-called capture range.

The capture-range in the multi-wavelengths technique depends mainly on the number of wavelength used, the central wavelengths and the errors. The plot in Figure 13 shows the values of the SHAPS capture range estimated for different filter combinations and with different piston errors.

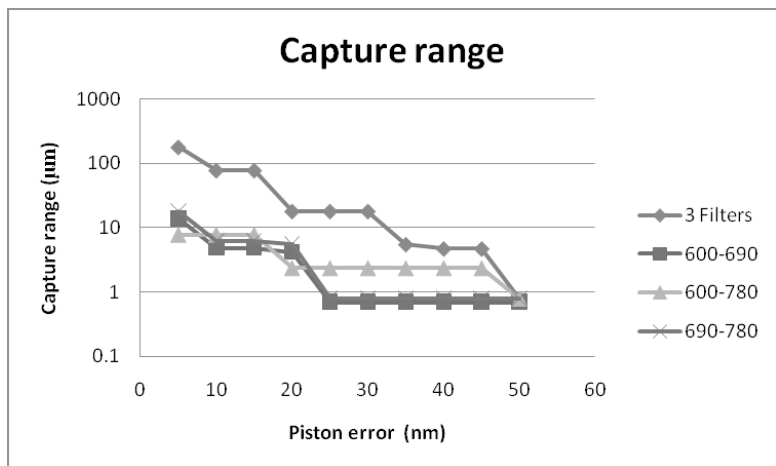


Figure 13: Capture range for different piston errors

The capture range increases with the precision of the measurement of the piston step. With a peak-to-valley measurement error of $\pm 5\text{nm}$, the capture range is 180μ when all 3 filters are used and between $8\mu\text{m}$ and $18\mu\text{m}$ when just 2 of them are used. For a peak-to-valley measurement error of 50nm , the capture range attains its minimum of λ for all combination of wavelengths. Note that in the case of 2 filters and for a measuring error $> 25\text{nm}$, the capture range is larger when the central wavelengths are further separated. It must be pointed out that the loss of coherence will probably prevent to measure piston steps larger than a few tens of microns.

5. PERFORMANCE OF SHAPS AT VLT

The theoretical precision that can be achieved by SHAPS in the measurement of the tilt of each segment can be computed using the following relation:

$$\delta_{\text{tilt}} = \frac{\sigma}{2\sqrt{N_{\text{lenslet}} \cdot N_{\text{phot}}}} \cdot \frac{1}{M}$$

where σ is the uncertainty in the estimation of the spot centroid in the focal plane of the lenslets, N_{phot} is the number of detected counts per lenslet, N_{lenslet} is the number of circular lenslets per segment (equal to 19) and M is the magnification between the lenslet array and the segmented mirror. The uncertainty has been assumed equal to $0.5 \frac{\lambda}{D}$, where λ is the wavelength and D is the lenslet diameter. In SHAPS, at 650nm , σ is approximately 2.25 mrad .

The theoretical precision that can be achieved by SHAPS in the measurement of the piston of each segment can be computed using the following relation (from [7]):

$$\delta_{\text{piston}} = \frac{\lambda}{\sqrt{2\pi} \sqrt{N_{\text{lenslet}} \cdot N_{\text{phot}}}} \cdot \frac{1}{2}$$

where the factor 2 is due to the reflection, N_{phot} is the number of counts per cylindrical lenslet and N_{lenslet} is the number of cylindrical lenslets per segment (approximately 2 on average).

The efficiency of SHAPS when operating on sky can be estimated as the product of the VLT efficiency ($\sim 70\%$, due to 3 reflections), the APE efficiency ($\sim 10\%$, due to more than 40 optical surfaces and the splitting of the beam into 4 parts) and the SHAPS efficiency ($\sim 50\%$ including the detector). This will give a total efficiency of SHAPS + APE at VLT of about 3.5% .

With the previous information it is possible to compute the theoretical precisions that can be achieved with SHAPS in the tilt and in the piston measurements as a function of the signal counts. The two curves are plotted in the Figure 14.

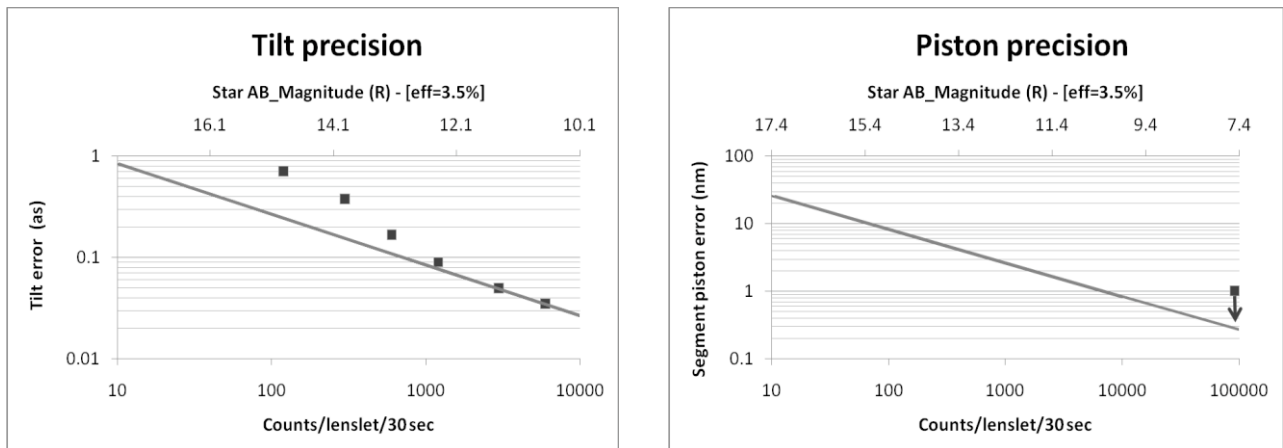


Figure 14: Expected tilt (left) and piston (right) precisions of SHAPS + APE at VLT. The points represent the values obtained during the preliminary tests.

The variable on the horizontal axis at the bottom is the number of the counts per lenslet for an integration time of 30 seconds, the variable on the horizontal axis at the top is the correspondent AB magnitudes of a star in R, assuming an overall efficiency (top of the sky – detector) of 3.5%, a reference wavelength of 650nm and a bandwidth of 50nm. The only noise considered here is the Poissonian photon noise.

The following table contains the values of the precisions at 4 intensities.

Counts per lenslet	AB Magnitude	Tilt precision (as)	Segment precision (nm)
10	17.5	0.83	25
100	15	0.26	8
1000	12.5	0.08	2.5
10000	10	0.026	0.8

The tilt precision achieved with the first measurements (see section 4.2) is in good agreement with the theoretical prediction for counts > 1000, when the photon noise dominates the detector noise. The piston precision achieved with the first measurement was better than 1 nm with about 10^5 counts per lenslet, which this represents an upper limit compliant with the prediction.

These predictions have been done for the diffraction limit case, without any disturbance due to atmospheric turbulence. Seeing will degrade the precision for the tilt and the piston measurement because of the smoothing of the signal.

The previous results can be extrapolated to the E-ELT, assuming the current configuration of SHAPS, i.e. 19 lenslets per segment with an aperture corresponding to 189 mm on sky. The main difference is the increase of the total efficiency by a factor ~ 10 due to the absence of APE. In that case the errors can be measured with the same precision as reported above but using stars which are 2.5 magnitudes fainter.

On the other hand, the increase of the number of segments (984 instead of 61, a factor ~ 16) and of the beam size will increase the size and complexity of the system: the opto-mechanical design of SHAPS should be scaled by a factor 4, maintaining the same accuracy in the alignment of the lenslet array, i.e. $15\mu\text{m}$ over a pupil size of 26mm in diameter. A 2K x 2K CCD might be sufficient to collect the full image with the same pixel scale of SHAPS. The memory requirement will increase by a factor 16^2 and the computing time (currently ~ 2 seconds) will increase by a factor somewhere in between 16^2 and 16, depending on the possibility to compute the heaviest calculations off-line. In 8 years from now, assuming that the computing power increases by a factor 2 per year, the hardware should be sufficiently fast to perform the computations in the same time currently needed by SHAPS.

6. CONCLUSIONS

In this paper the new optical layout and the opto-mechanical design of SHAPS have been presented together with the algorithms used in the wavefront analysis to compute the coefficients of the aberrations, of the segment tip-tilts and piston steps.

The results obtained during the preliminary tests performed in the laboratory are presented. It has been shown that currently SHAPS is able to measure the continuous aberration and to compute the tip-tilts and the pistons of the segments with the theoretically expected precision. The full characterization of SHAPS and the test on sky at VLT are the main tasks for the next months.

The performances of SHAPS with APE at the VLT are estimated as functions of the signal counts and of the magnitude of the reference star. These performances have been extrapolated to the E-ELT case, where the increase of the total efficiency will permit to achieve the same precision on stars which are 2.5 magnitudes fainter.

ACKNOWLEDGMENTS

SHAPS is a subsystem of the experiment APE which is financed by the European Union and the European Southern Observatory via the Sixth European Union Framework Program for research and technological development under the contract number 011863.

REFERENCES

1. Andolfato, L., Karban, R., “Workstation Software Framework”, ref. 7019-74, this Conference.
2. Chanan, G.A., Troy, M., et al., “Phasing the mirror segments of the Keck telescopes: the broadband phasing algorithm,” *Appl. Opt.* 37, 140 (1998).
3. Gontè, F., et al., “Shack-Hartmann Sensor for the Active Phasing Experiment,” in *Ground-based and Airborne Telescopes*, L. Stepp, ed. Proc. SPIE 6267, 626730, (2006).
4. Gontè, F., et al., “Active Phasing Experiment: preliminary results,” ref. 7012-34, this Conference.
5. Platt, B., C., Shack, R., “History and Principle of Shack-Hartmann Wavefront sensing,” *Journal of Refractive Surgery*, Vol. 17, (2001).
6. Mazzoleni, R., & al., “Disentangling between low order telescope aberrations and segmentation errors using a Shack-Hartmann sensor,” ref. 7012-41, this Conference.
7. Noethe, L., Adorf, H.-M., “Optical measurements of phase steps in segmented mirrors—fundamental precision limits,” *Journal of Modern Optics*, vol. 54, issue 1, (2007)
8. Löfdahl, M., Eriksson, H., “An algorithm for resolving 2 ambiguities in interferometric measurements by use of multiple wavelengths,” *Opt. Eng.* 40, 2019–2058 (2001).
9. Yaitskova, N., & al, “The Active Phasing Experiment Part I: Concept and Objectives,” in *Ground-based and Airborne Telescopes*, L. Stepp, ed. Proc. SPIE 6267, 62672Z, (2006).